Z. Phys. Chem. / **DOI** 10.1524/zpch.2013.0406

Electron-Transfer-Induced Dissociation of H_2 on Gold Nanoparticles: Excited-State Potential Energy Surfaces *via* Embedded Correlated Wavefunction Theory

By Florian Libisch[1], Jin Cheng[2], and Emily A. Carter[3,*]

[1] Department for Mechanical and Aerospace Engineering, Princeton University, Engineering Quadrangle, Olden Street, NJ, 08540 Princeton, USA
[2] Department of Chemistry, Princeton University, Washington Road, NJ, 08544 Princeton, USA
[3] Department for Mechanical and Aerospace Engineering, Program in Applied and Computational Mathematics, and Andlinger Center for Energy and the Environment, Princeton University, Engineering Quadrangle, Olden Street, NJ, 08540 Princeton, USA

(Received February 27, 2013; accepted in revised form April 23, 2013)
(Published online July 8, 2013)

Plasmons / Photocatalysis / Potential Energy Surfaces

Noble metal surfaces play a central role in heterogeneous catalysis. Lasers of the appropriate resonance frequency efficiently generate surface plasmons. These, in turn, may generate hot electrons, which can drive catalytic reactions at low temperatures. In this work, we demonstrate how embedding methods allow for the use of accurate *ab-initio* correlated wavefunction methods to describe excited-state potential energy surfaces of molecule–surface interactions. As model system, we consider the hot-electron-induced dissociation of hydrogen on Au(111), which has recently been demonstrated experimentally. We discuss merits and limitations of several different correlated wavefunction schemes. Our results show that dissociation barriers may be substantially reduced upon electron excitation and suggest a method to calculate the hot electron energies required for catalytic reactions.

1. Introduction

The interaction of molecules with transition metal surfaces is central to much of heterogeneous catalysis [1]. Ongoing research aims for efficient low-temperature catalysis at ambient conditions, to reduce unwanted side reactions and prolong catalyst lifetime. Plasmon-induced catalysis promises to achieve these goals: in recent years, research groups have demonstrated, *e.g.*, plasmon-driven H_2 production from alcohol [2,3], liquid-phase water splitting [4–6], gas-phase oxidation reactions [7,8], and

* Corresponding author. E-mail: eac@princeton.edu

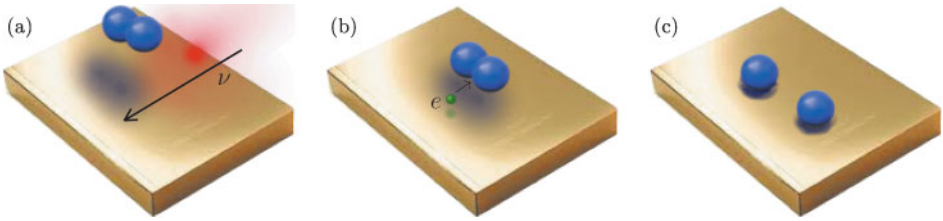

Fig. 1. H_2 dissociation on a gold surface by a plasmon-induced hot electron: (a) incoming photon ν (red) generates (b) a hot electron e (green), that jumps into the antibonding orbital of a physisorbed H_2 molecule (blue), (c) leading to dissociation.

hydrocarbon conversion [9]. In particular, noble-metal nanoparticles comprise an excellent source of hot electrons [10–13]. The electrons couple strongly with light of suitable frequencies, generating collective excitations of surface electrons, so-called surface plasmons. These quickly decay, leading to reemission of photons, or the creation of single electron–hole pair excitations, depending on nanoparticle size. In the latter case, the energy of the resulting hot electron directly relates to the initial plasmon energy. Since surface plasmon energies can be varied over a wide range of frequencies by choosing suitable noble metals and nanoparticle shapes and sizes, such nanoparticles offer an excellent way to generate hot electrons of specific energy at high throughput and low energy requirements. As shown for the oxidation of CO on Ru(0001), hot electrons can chemically activate adsorbates [14], driving chemical processes. As a proof of principle, plasmons from Au nanoparticles were recently used to efficiently generate hot electrons, that subsequently enabled hydrogen dissociation (see Fig. 1) [15].

Tailoring of hot-electron energies by tuning the nanoparticle plasmon resonance is readily possible. One could thus envision to efficiently and selectively enhance catalytic reactions by aiming for the energies of antibonding orbitals in target molecules. Such a proposal requires reliable theoretical methods to predict said energies, for molecules chemisorbed or physisorbed on the surface. Unfortunately, despite the importance of heterogeneous catalysis, the details of the elementary processes involved remain poorly understood [16,17]. Density functional theory (DFT), the workhorse of first principles electronic structure calculations, is well suited to describe extended metal surfaces, but fails to correctly account for charge transfer [18]. Furthermore, the theoretical modeling of plasmon-induced hot electrons requires treating excited states. Although the linear-expansion delta self-consistent field extension of DFT (Δ SCF-DFT) [19] has been used to approximate excited-state potential energy surfaces (PESs) in order to model hot-electron interactions with adsorbates [20,21], a more accurate treatment is beyond the scope of a ground state theory like DFT. In turn, highly accurate correlated wavefunction (CW) methods are restricted to comparatively small numbers of electrons due to their unfavorable scaling with system size. In the present manuscript, we show how quantum-mechanical embedding methods can be used to combine both theories. We apply our method to the hot-electron-induced dissociation of H_2 on gold (see Fig. 2). We find a strong reduction in the effective barrier height at specific excitation energies, corresponding to a Feshbach resonance of H_2^-. Technical details, different adsorption sites, and possible applications to more complicated cases are also presented.

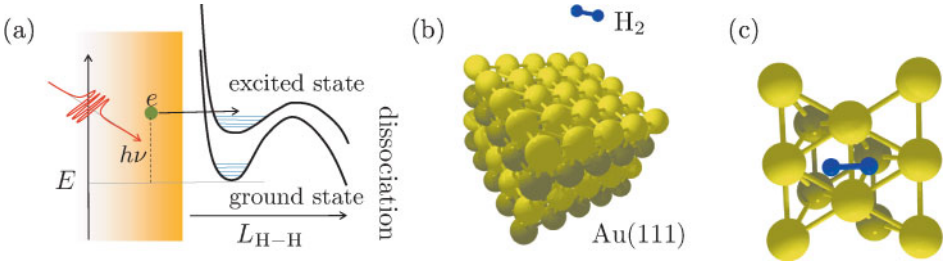

Fig. 2. (a) Schematic view of plasmon-driven H_2 dissociation energetics: incoming photon ($h\nu$) excites a surface plasmon, which in turn decays into a hot electron (see Fig. 1). This electron may transfer into an antibonding state of an approaching molecule (horizontal arrow), which ultimately leads to dissociation. (b) Au (111) slab and approaching H_2 used in periodic DFT. (c) Approaching H_2 molecule and Au_{12} cluster used in our embedded correlated wavefunction calculations.

This paper is organized as follows. In the next section, we review our theoretical methods, *i.e.*, the embedding framework and quantum chemistry techniques we use to model hot-electron-induced surface catalysis, outlining computational challenges, particularly the treatment of excited states and basis set choice. We then discuss ground and excited state PESs for H_2 dissociation on Au(111) obtained with different levels of theory in Sect. 3. We conclude with a short summary and an outlook.

2. Theory

We aim to calculate the *ab-initio* PESs, and thus reaction barriers, for the ground and several excited states of a gold (111) surface interacting with an approaching H_2 molecule (Fig. 2a). We want to describe the hot electrons generated by plasmons on the Au (111) nanoparticle surface close to the adsorption point, and the H_2 molecule, using *ab-initio* CW methods. These techniques are too expensive to treat large nanoparticles and do not support the periodic boundary conditions required for surface slab calculations. To circumvent this problem, we use quantum mechanical embedding: we carve a 12-atom gold nanocluster out of a gold (111) surface (see Fig. 2c). We then determine on the DFT level a unique, local embedding potential V_{emb}, that mediates the interaction between the cluster and the remaining (infinitely extending) metal surface [22]. CW methods incorporating V_{emb} can then be used to treat the dissociation of H_2 on the embedded Au cluster. Note that we do not consider here the dynamics of the dissociation process, in particular the non-adiabatic entanglement between the ground and excited hydrogen states. Including such effects requires an Anderson–Newns-type Hamiltonian [23], which includes a nonadiabatic coupling between the hot electron and the hydrogen coordinates [21]. We hope, however, that the PESs obtained using our embedding method may serve as a basis for future modeling in this direction.

Concerning cluster size and geometry, we choose a twelve-atom cluster (see Fig. 2c) to balance between numerical accuracy and speed: to avoid unpaired electrons in the cluster that might produce artificial spin-polarization, we consider an even number of atoms. To correctly model charge rearrangement at the metal surface due to the

image charge effect, we want to maximize the surface area covered by the cluster's top layer, which therefore includes eight atoms. In similar calculations for the dissociation of dioxygen on Al(111) [35] we find that too-small clusters overestimate the cost of charge transfer (due to the fixed, finite number of electrons in the cluster), and thus the energy cost for dissociation. On the other hand, larger cluster sizes quickly become unfeasible to treat with CW methods. Since the screening length of well conducting metals like gold is of the order of 0.5 Å [24], much smaller than the cluster size, we expect that the errors due to the finite cluster size are small. The same twelve-atom cluster model used here exhibited, for the aluminum case, converged results for the related charge-transfer-induced dioxygen dissociation barrier with respect to cluster size (for details, see also the supplement of [35]). To include self-consistent charge exchange between cluster and the remaining metal surface requires, *e.g.*, a potential-functional embedding approach [25]. The latter is, however, computationally very demanding, since the embedding potential has to be reevaluated in a self-consistency cycle for each hydrogen position.

To determine the embedding potential, we calculate the DFT ground state density ρ_{ref} of an Au(111) periodic slab using a 5×5 supercell in the surface plane and four layers in the [111] direction, with 100 atoms in the supercell and 20 Å of vacuum buffer between periodic images (see Fig. 2b), using the ABINIT code [26]. We use Perdew–Burke–Ernzerhof (PBE) exchange-correlation (XC) [27], a Trouiller–Martins generalized gradient approximation (GGA) [28] pseudopotential for Au, a plane-wave (PW) cutoff of 700 eV, and a $3 \times 3 \times 1$ Monkhorst–Pack grid for k-point sampling. For all PW DFT calculations, we employ Fermi–Dirac smearing of 0.1 eV. We then partition this bare slab into a small two-layer Au_{12} cluster (see Fig. 2c) and the remainder considered as the environment. Both subsystems are solved independently, with the same setup, in the presence of V_{emb}, yielding ground state densities ρ_{clu} and ρ_{env}. Consider the functional [29]

$$W[V_{\text{emb}}] := E[\rho_{\text{cl}}] + E[\rho_{\text{env}}] + \int V_{\text{emb}} \left[\rho_{\text{cl}} + \rho_{\text{env}} - \rho_{\text{ref}}\right] . \tag{1}$$

The gradient $\delta W / \delta V_{\text{emb}} = \rho_{\text{cl}} + \rho_{\text{env}} - \rho_{\text{ref}}$, since ρ_i, $i = \{\text{cl}, \text{env}\}$ are the ground state densities, and thus $\delta E / \delta \rho_i = 0$ [29]. This gradient obviously vanishes at $\rho_{\text{cl}} + \rho_{\text{env}} = \rho_{\text{ref}}$, where V_{emb} is converged and W is maximal [29]. We can thus determine V_{emb} by, *e.g.*, L-BFGS optimization [30]. This algorithm has been implemented in a modified version of the ABINIT code [26].

V_{emb} is then supplied to modified versions of MOLCAS [31] (for embedded complete active space self consistent field (CASSCF)) and GAMESS [32] (for embedded configuration interaction (CI) singles) codes operating on the embedded cluster. We use an eight electrons in eight orbitals active space: the bonding and antibonding H_2 orbitals, as well as three HOMOs and three LUMOs from the Au cluster. We have verified that a CAS(10/10) or CAS(6/6) yields very similar results. To obtain the CW-corrected final energy

$$E_{\text{emb}} = E^{\text{DFT}} + E^{\text{CW}}_{\text{emb}} - E^{\text{DFT}}_{\text{emb}} , \tag{2}$$

we additionally require an embedded Kohn–Sham (KS)-DFT calculation using GAMESS. Both embedded DFT and CW calculations use the same Gaussian basis set,

resulting in favorable cancellation of basis set errors. We discuss the details of basis set choice below.

For a baseline DFT description of the ground state PES, we use projector-augmented-wave (PAW) calculations as implemented in the VASP code version 5.2 [33], including the new (2012) PAW potentials for Au and H. In these calculations, we also employ the PBE XC functional [27]. We model the Au(111) surface by a periodic 3×3 supercell containing seven Au layers separated by 20 Å of vacuum for a total of 63 atoms, and a $6 \times 6 \times 1$ Monkhorst–Pack grid for *k*-point sampling (due to the large supercell, this is enough for a converged calculation). The PAW formalism allows for minimal cutoffs of 172 and 200 eV for Au and H potential respectively, in contrast to substantially larger cutoffs required for, *e.g.*, the ABINIT calculations to determine V_{emb}. The higher energy cutoff for hydrogen is due to the short-range potential of the unscreened hydrogen core. For higher accuracy, we use a plane wave cutoff of 250 eV. To eliminate dipole interactions, a mirrored hydrogen molecule is added on the other side of the slab. We perform a spin-polarized calculation to allow for charge transfer.

Due to the strong variations of density close to the hydrogen cores, convergence of the PW calculation is not trivial. As recommended for metal slab calculations, we adjust the mixing parameters for the self-consistency cycle [34]. Additionally, we need to preconverge using the conjugate gradient algorithm (`ALGO=A LSUBROT=FALSE TIME=0.1`) implemented in VASP, as other algorithms will cause excessive charge sloshing, with no convergence.

2.1 Excited states

Since we are interested in the description of plasmon-induced hot electrons, we require the modeling of excited states. Our previous work [35] employed complete active space descriptions, including second-order multi-reference many-body perturbation theory, CASPT2. For the problem at hand, however, the optimization of the ground state orbitals employed in the CASSCF optimization proves detrimental to the description of highly excited states: their characteristics might not be well resolved by the optimized ground state orbitals. State averaging (*i.e.*, the inclusion of excited states in the optimization process) can be easily introduced to describe a few excited states. Indeed, we find state averaging over at least two states is necessary to achieve smooth PESs. However, we are interested in high-lying excitations. Unfortunately, state averaging over ten states already becomes numerically cumbersome, especially for the CASPT2 calculations. We thus want to consider alternative CW approaches. CI methods promise correct modeling of excited states. However, their unfavorable scaling makes the treatment of nanoclusters with 12 Au atoms unfeasible using, *e.g.* multi-reference single and double excitation CI (MRSDCI) calculations. Smaller clusters for which MRSDCI would be tractable tend to overestimate reaction barriers as charge lost to the adsorbed molecule is not sufficiently screened [35]. A potential alternative approach is CI Singles (CIS, *i.e.*, treating all possible single excitations), which has been shown to treat excited states well, as long as they do not involve any double excitations [36]. An embedded CIS calculation for the Au_{12} cluster is numerically challenging, but feasible. We expect single excitations involving electron transfer from the metal cluster to the H_2 molecule to dominate the excited state spectrum. Furthermore, we want to model singly

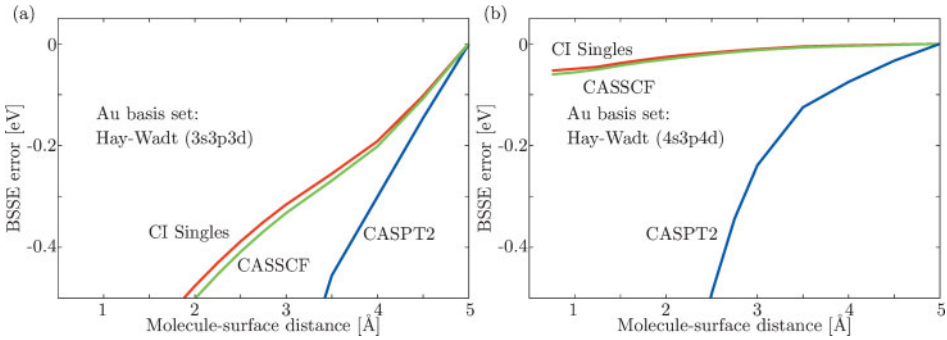

Fig. 3. Counterpoise correction obtained by approaching the Au_{12} cluster at the bridge site (Fig. 2c) with a ghost hydrogen molecule oriented parallel to the cluster surface (aug-cc-pVTZ basis set) at different levels of theory (see insets). We tested two different Hay–Wadt basis sets for Au: (a) uncontracted (3*s*3*p*3*d*) and (b) introducing additional *s* and *d* diffuse functions (see text), for a final (4*s*3*p*4*d*) basis set.

excited hot electrons. Consequently, we expect a CIS description to work well for the system at hand. Nevertheless, we will compare CASSCF, CASPT2, and CIS approaches below.

2.2 Basis set choice

We use a Dunning aug-cc-pVTZ diffuse basis set for H [37], and an uncontracted (3*s*3*p*3*d*) Hay–Wadt basis set accompanying an effective core potential (ECP) for the Au atoms [38]. Naïve calculations using these basis sets, Eq. (2) and CASPT2 surprisingly predict direct adsorption of H_2 on Au nanoclusters, strongly contradicting both DFT [39] and experimental evidence [15]. While both embedded DFT and embedded CASSCF predict an increase in energy upon approaching the surface, the CASSCF energy increases much more slowly, wrongly suggesting additional contributions to correlation that favor hydrogen adsorption. The situation is even more severe with CASPT2, where the ground state CASPT2 PES implies chemisorption. Closer examination reveals a strong dependence of the CASSCF energy on the Au basis set for small Au–H_2 distances $L_{\text{Au–H}_2}$: since we use a Dunning basis set with diffuse functions for H_2, Au *d* electrons may lower their energy by using the hydrogen basis functions. This is confirmed by evaluating the basis set superposition error (BSSE) using the counterpoise correction (CPC) of Boys and Bernardi [40]: we replace either the Au cluster, or the H_2 molecule, by ghost atoms featuring the same basis set but no electrons or nucleus. Our results show that the energy of the embedded Au cluster strongly depends on the distance of the ghost hydrogen molecule (see Fig. 3a). The correction is especially large for CASPT2. To reduce this problem, we add diffuse basis functions (featuring exponents of 0.006415 and 0.0455 for *s* and *d* respectively) to the four Au atoms closest to the adsorption site. This measure strongly reduces the CPC for all levels of theory (see Fig. 3b). Applying the CPC to the final PES recovers the expected, physical repulsion of H_2 by Au(111). Unfortunately, while the ground state PES can be corrected properly by the CPC, the correction does not directly apply to excited states: electronically excited states of the full problem and of the ghost-atom calculations needed for the CPC

cannot be related. Consequently, due to the large BSSE of many-body perturbation theory (*i.e.*, CASPT2) applied to tractable-sized basis sets, we further restrict ourselves in the discussion of excited states to CIS and CASSCF calculations, for which the BSSE is very small as long as the extra Au diffusion functions are used. We stress here that this is not a consequence of the embedding approach: isolated clusters show the same problem of strongly overestimating the binding energy of H_2.

3. Results

H_2 in vacuum features a binding energy of ≈ 4.5 eV whereas the H_2^- anion is only bound by ≈ 2.2 eV [41]. For small H–H bond lengths $L_{\mathrm{H–H}}$, H_2^- becomes unstable towards ejection of an electron, $H_2^- \rightarrow H_2 + e$. Conversely, H_2 features a metastable Feshbach resonance at 1.7 eV corresponding to occupation of the σ^* orbital [41]. Upon approaching a Au (111) surface parallel to the surface (see Fig. 2), the ground state potential energy surface obtained using pure KS DFT features a steep rise in energy. Favorable interaction of the σ orbital with the partially filled *sp* band of Au(111) not only decreases the H_2 orbital energy, it ultimately shifts the antibonding σ^* orbital below the Fermi energy [39]. Accordingly, a charge analysis reveals that the H_2 molecule becomes negatively charged as it approaches the surface, corresponding to a partial occupation of the σ^* antibonding orbital. The energy gain by interaction with the Au *sp* surface electrons is offset by the energy cost to orthogonalize to the *d*-band surface state. The latter cost along with the partial occupation of σ^* leads to a net increase in energy as H_2 approaches. Indeed, we find, for all levels of theory, a gradually increasing negative charge on the H_2 with decreasing $L_{\mathrm{Au–H_2}}$. Due to the energy cost of occupying σ^*, H_2 does not normally adsorb (or dissociate) on a smooth Au(111) surface [39], making this model system well suited to isolate plasmon-driven reactions.

At a bond length $L_{\mathrm{H–H}} \approx 1.2$ Å, we find a saddle point within DFT at an H_2-surface distance $L_{\mathrm{Au–H_2}} \approx 1.2$ Å (see white arrow in Fig. 4a), with an associated reaction barrier towards dissociation of 1.35 eV. The measured temperature dependence of the dissociation yield on gold nanoclusters suggests a lower effective barrier [15]. However, comparison to experiment proves difficult: the experimental setup features an additional surrounding TiO_2 layer, as well as many more facets than the (111) surface. Both of these should lower the dissociation barrier: the former because the TiO_2 substrate slightly increases the Fermi level in the gold cluster, favoring charge transfer [42]. The observation of much higher catalytic activity of smaller nanoclusters [43] further corroborates the importance of defects and facet boundaries in experiment. Indeed, there is a finite base reaction count in experiment at zero laser power (no plasmon generation), that would not be present for an ideal Au (111) surface [15]. Consequently, since we investigate an ideal Au surface and neglect the TiO_2 substrate, we expect a larger barrier than experiment.

Using the embedding framework for calculating a CW-corrected ground state PES for the molecule approaching parallel to the Au(111) surface, we obtain qualitatively similar results for state-averaged emb-CASSCF and emb-CIS, while emb-CASPT2 features a reduced barrier located at smaller $L_{\mathrm{H–H}}$ (all with BSSE CPC; see Fig. 4b–d, as well as Table 1). Towards larger $L_{\mathrm{H–H}}$, the emb-CIS energy increases more quickly than

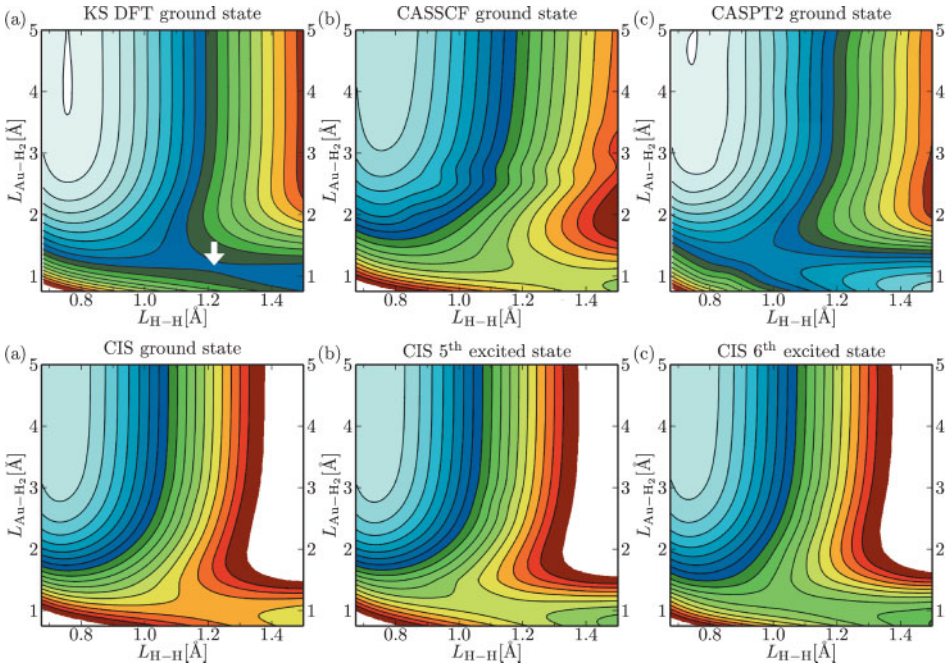

Fig. 4. Potential energy surfaces for different levels of theory: (a) KS-DFT (white arrow marks barrier towards dissociation); (b) ground state CASSCF, state-averaged over the 10 lowest-lying roots, using a CAS (8,8); (c) CASPT2 correction of (b); (d) CIS ground state, as well as (e) fifth and (f) sixth excited state [15]. Contour line separation is 160 meV.

Table 1. DFT and embedded CW predictions of ground and excited state barrier heights (all energies in eV) and positions of the top of the barrier. BSSE corrections included for all ground state embedded CW calculations. Emb-CASPT2 results for the excited state excluded due to the large BSSE error (see text).

	E_0^{Barrier}	E_6^{Barrier}	$L_{\mathrm{H-H}}^{\mathrm{Barrier}}$ [Å]	$L_{\mathrm{Au-H_2}}^{\mathrm{Barrier}}$ [Å]
DFT-GGA	1.35	–	1.2	1.2
emb-CASPT2	1.20	–	1.0	1.2
emb-CIS	2.30	1.70	1.1	1.0
emb-CASSCF	2.00	1.95	1.3	1.0
CASSCF $V_{\mathrm{emb}} \equiv 0$	2.40	2.10	1.2	1.1

the others, leading to a larger cost to break the bond. This is to be expected for our CIS ansatz, as the ground state is a single-reference Hartree–Fock solution that overestimates the cost of bond breaking. Close to the surface, CASPT2 predicts much smaller barrier heights, even with the BSSE CPC. We conjecture that this low CASPT2 value might be related to a still too small basis set: the large BSSE for CASPT2 suggests that the perturbative expansion strongly amplifies the BSSE error, for which the first-order CPC fails to completely account. At the top of the barrier, a charge of about 0.8*e*

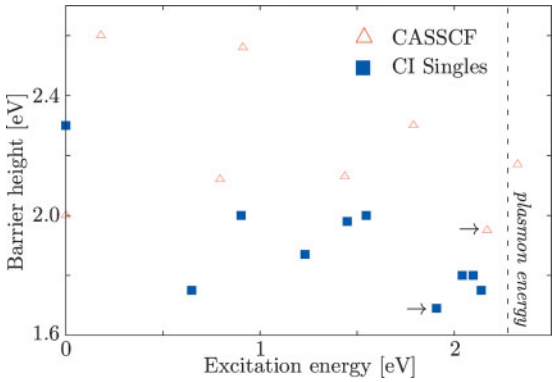

Fig. 5. Excited state energies relative to the ground state (x-axis) and associated dissociation barrier heights (y-axis) for eigenstates of embedded CASSCF (red triangles) and embedded CIS (blue squares). Lowest barrier for sixth excited state in both theories (marked by arrows). Plasmon energy in experiment marked by a dashed line [15].

(± 0.1 depending on level of theory and charge analysis) transfers from the Au cluster to H_2. This amount of charge transfer is, with fluctuations of $< 10\%$, observed for all excited state PESs that we investigated. Put differently, exciting the gold cluster does not induce a charge-transfer state, but rather changes the energy cost of initiating charge transfer. Note that an H_2 molecule approaching the surface in a perpendicular orientation merely yields a repulsive PES, with no indication of dissociation or abstraction (not shown).

For state-averaged CASSCF and CIS, we also calculate nine excited states (we do not consider CASPT2 for the excited states because of the BSSE for which there is no obvious CPC, as mentioned earlier). We find that different excited states of the H_2/embedded cluster system feature quite different heights of the dissociation barrier (see Fig. 5). On average, CIS predicts a larger decrease in energy, again probably because of the comparatively low-level ground-state SCF ansatz. However, since CIS considers all possible single excitations, we find a smaller energy spacing between excited states (or, put differently, more excited states are in the energy window of up to 2.5 eV) than for CASSCF. Since the metal cluster features many quasi-degenerate (metallic) energy levels at the Fermi level, this is not easily corrected by slowly enlarging the CAS (we have explicitly done up to CAS 12/12 calculations with no substantial change). We observe the same qualitative trend in both theories: three excitation energy regions with comparatively small barriers at about 0.7, 1.3, and 1.9 eV. Quantitatively, CIS consistently features lower barriers towards dissociation, probably because all single excitations into the many LUMOs of the cluster are considered. For both theories, the lowest barrier is found at an excitation energy of around 2 eV (see arrows in Fig. 5), which is slightly below the experimental photon energy (2.3 eV). The barrier at an excitation energy of 0.7 eV is only slightly higher, and could potentially allow a laser with lower energy (and associated engineered nanoparticles with a smaller resonance frequency) to drive hydrogen dissociation with even lower power consumption.

Finally, we want to compare our embedding framework to CW calculations on bare clusters (*i.e.*, without embedding): we find much too large dissociation barriers (of the order of 3.5 eV), with the top of the barrier occurring at a bond length of $L_{\mathrm{H-H}} = 1.5$ Å. On the other hand, using a simplified ONIOM model [44] (*i.e.*, using equation (2) for the final energy, but neglecting the embedding potential, $V_{\mathrm{emb}} = 0$) yields qualitatively similar results than the embedding framework. However, barrier heights and excited state energies change considerably (of the order of 20%), and the barrier height is overestimated, see Tab. 1. Finally, the PES becomes much more bumpy than a PES using our embedding framework, presumably because the bare cluster electron density is more easily polarized by the hydrogen molecule than the embedded cluster, which is modulated by the embedding potential that represents the extended metal surface.

4. Conclusions

In summary, we have shown how to obtain PESs for molecules interacting with locally excited extended metal surfaces. We discuss problems involving too small Gaussian basis sets, and investigate different levels of CW theory. We find that CASPT2 is, at least for this system and level of basis set, quite susceptible to BSSE. CIS furnishes a valuable, comparatively cheap alternative for the investigation of excited states to more costly CASSCF or MRSDCI methods, with minimal BSSE.

The potential energy surface for H_2 approaching Au(111) features a dissociation barrier involving a charge-transfer state, that varies in height for different electronic excitations of the metal: by exciting hot electrons at the surface of the metal, the cost for charge transfer to reach the transition state is lowered, increasing the dissociation rate. Our CIS results suggest that lower-energy photons should also be suited to drive the reaction, requiring less laser power. We hope that the PESs obtained using our embedded correlated wavefunction treatment of excited states can be used as a basis for more sophisticated descriptions of the interaction between electronic and nuclear degrees of freedom [21].

Acknowledgement

We thank C. Huang, G. Kresse, S. Mukherjee, and P. Nordlander for valuable discussions. We gratefully acknowledge support from the Office of Naval Research and the National Science Foundation. Calculations were performed on the CSES high performance computing cluster at Princeton University, and on the Vienna Scientific Cluster.

References

1. P. A. Kilty and W. M. H. Sachtler, Cat. Rev. Sc. Eng. **10** (1974) 1.
2. M. Murdoch, G. I. N. Waterhouse, M. A. Nadeem, J. B. Metson, M. A. Keane, R. F. Howe, J. Llorca, and H. Idriss, Nat. Chem. **3** (2011) 6.
3. Z. W. Seh, S. Liu, M. Low, S.-Y. Zhang, Z. Liu, A. Mlayah, and M.-Y. Han, Adv. Mater. **24** (2012) 2310.
4. J. Lee, S. Mubeen, X. Ji, G. D. Stucky, and M. Moskovits, Nano Lett. **12** (2012) 5014.

5. C. G. Silva, R. Juarez, T. Marino, R. Molinari, and H. J. Garcia, Am. Chem. Soc. **133** (2011) 595.
6. D. B. Ingram, and S. J. Linic, Am. Chem. Soc. **133** (2011) 5202.
7. P. Christopher, H. Xin, and S. Linic, Nature Chem. **3** (2011) 467.
8. W. H. Hung, M. Aykol, D. Valley, W. Hou, and S. B. Cronin, Nano Lett. **10** (2010) 1314.
9. W. Hou, W. H. Hung, P. Pavaskar, A. Goeppert, M. Aykol, and S. B. Cronin, ACS Catal. **1** (2011) 929.
10. M. W. Knight, H. Sobhani, P. Nordlander, and N. J. Halas, Science **332** (2011) 6030.
11. I. Goykham, Desiatov, J. Khurgin, J. Shappir, and U. Levy, Nano Lett. **11** (2011) 2219.
12. Z. Fang, Z. Liu, Y. Wang, P. M. Ajayan, P. Nordlander, and N. J. Halas, Nano Lett. **12** (2012) 3808.
13. Z. Fang, Y. Wang, Z. Liu, A. Schlather, P. M. Ajayan, F. H. L. Koppens, P. Nordlander, and N. J. Halas, ACS Nano **6** (2012) 10222.
14. M. Bonn, S. Funk, Ch. Hess, D. N. Denzler, C. Stampfl, M. Scheffler, M. Wolf, and G. Ertl, Science **285**, 1042 (1999).
15. S. Mukherjee, F. Libisch, N. Large, O. Neumann, L. V. Brown, J. Cheng, B. Lassiter, E. A. Carter, P. Nordlander, and N. J. Halas, Nano Lett. **13** (2013) 240.
16. G.-J. Kroes, Science **321** (2008) 794.
17. T. Zambelli, J. V. Barth, J. Wintterlin, and G. Ertl, Nature **390** (1997) 495.
18. J. P. Perdew, M. Levy, and J. L. Balduz, Phys. Rev. Lett. **49** (1982) 1691.
19. J. Gavnholt, T. Olsen, M. Engelund, and J. Schiøtz, Phys. Rev. B **78** (2008) 075441.
20. P. Christopher, H. Xin, A. Marimuthu, and S. Linic, Nat. Mater. **11** (2012) 1044.
21. T. Olsen, J. Gavnholt, and J. Schiøtz, Phys. Rev. B **79** (2009) 035403.
22. C. Huang, M. Pavone, and E. A. Carter, J. Chem. Phys. **134** (2011) 154110.
23. P. W. Anderson, Phys. Rev. **124** (1961) 41; D. M. Newns, Phys. Rev. **178** (1969) 1123.
24. J. Feinleib, Phys. Rev. Lett. **16**, 1200 (1966).
25. C. Huang and E. A. Carter, J. Chem. Phys. **135**, 194104 (2011).
26. X. Gonze, B. Amadon, P.-M. Anglade, J.-M. Beuken, F. Bottin, P. Boulanger, F. Bruneval, D. Caliste, R. Caracas, M. Côté, T. Deutsch, L. Genovese, Ph. Ghosez, M. Giantomassi, S. Goedecker, D. R. Hamann, P. Hermet, F. Jollet, G. Jomard, S. Leroux, M. Mancini, S. Mazevet, M. J. T. Oliveira, G. Onida, Y. Pouillon, T. Rangel, G.-M. Rignanese, D. Sangalli, R. Shaltaf, M. Torrent, M. J. Verstraete, G. Zerah, and J. W. Zwanziger, Comp. Phys. Commun. **180** (2009) 2582; X. Gonze, G.-M. Rignanese, M. Verstraete, J.-M. Beuken, Y. Pouillon, R. Caracas, F. Jollet, M. Torrent, G. Zerah, M. Mikami, P. Ghosez, M. Veithen, J.-Y. Raty, V. Olevano, F. Bruneval, L. Reining, R. Godby, G. Onida, D. R. Hamann, and D. C. Allan, Zeit. Kristallogr. **220** (2005) 558.
27. J. P. Perdew, K. Burke, and M. Ernzerhof, Phys. Rev. Lett. **77** (1996) 3865.
28. N. Troullier and J.-L. Martins, Phys. Rev. B **43** (1993) 1991.
29. Q. Wu and W. Yang, J. Chem. Phys. **118** (2003) 2498.
30. C. Zhu, R. H. Byrd, P. Lu, and J. Nocedal, ACM Trans. Math. Software **23** (1997) 550; J. Nocedal and J. L. Morales, ACM Trans. Math. Software **38** (2011) 7.
31. F. Aquilante, L. De Vico, N. Ferré, G. Ghigo, P. Malmqvist, P. Neogrády, T. B. Pedersen, M. Pitoňák, M. Reiher, B. O. Roos, L. Serrano-Andrés, M. Urban, V. Veryazov, and R. Lindh, J. Comput. Chem. **31** (2010) 224.
32. M. W. Schmidt, K. K. Baldridge, J. A. Boatz, S. T. Elbert, M. S. Gordon, J. H. Jensen, S. Koseki, N. Matsunaga, K. A. Nguyen, S. Su, T. L. Windus, M. Dupuis, and J. A. Montgomery Jr, Comput. Chem. **14** (1993) 1347; M. S. Gordon, *Theory and Applications of Computational Chemistry: the First Forty Years*, Elsevier, Amsterdam (2005).
33. J. Kresse and J. Furthmüller, Comp. Mater. Sci. **6** (1996) 15.
34. G. Kresse, M. Marsman, and J. Fürthmüller, VASP the guide, Computational Physics, Faculty of Physics, Universität Wien, Vienna, Austria, http://cms.mpi.univie.ac.at/vasp/vasp/vasp.html, 2009.
35. F. Libisch, C. Huang, P. Liao, M. Pavone, and E. A. Carter, Phys. Rev. Lett. **109** (2012) 198303.
36. K. D. Closser and M. J. Head-Gordon, Phys. Chem. A **114** (2010) 8023.

37. T. H. Dunning Jr., J. Chem. Phys. **90** (1989) 1007.
38. P. J. Hay and W. R. Wadt, J. Chem. Phys. **82** (1985) 270.
39. B. Hammer and J. K. Norskov, Nature **376** (1995) 238.
40. S. F. Boys and F. Bernardi, Mol. Phys. **19** (1970) 553.
41. R. McWeeny, J. Mol. Struc.-THEOCHEM **261** (1992) 403.
42. S. Laursen and S. Linic, Phys. Rev. Lett. **97** (2006) 026101.
43. N. Lopez, T. V. W. Janssens, B. S. Clausen, Y. Xu, M. Mavrikakis, T. Bligaard, and J. K. Nørskov, J. Catal. **223** (2004) 232; E. Roduner, ChemInform **37** (2006) DOI:10.1002/chin.200639226; ; B. Hvolbæk, T. V. W. Janssens, B. S. Clausen, H. Falsig, C. H. Christensen, and J. K. Nørskov, Nano Today **2** (2007) 14.
44. M. Svensson, S. Humbel, R. D. J. Froese, T. Matsubara, S. Sieber, and K. Morokuma, J. Phys. Chem. **100** (1996) 19357.